RESEARCH ARTICLE

Check for updates

ADVANCED
OPTICAL
MATERIALS

www.advopticalmat.de

Engineering Waveguide Nonlinear Effective Length via Low Index Thin Films

Wallace Jaffray, Farhan Ali, Sven Stengel, Ziheng Guo, Sebastian A. Schulz, Andrea Di Falco, and Marcello Ferrera*

Novel photonic nanowires are fabricated using low-index materials and tested in the near-infrared spectrum to assess their nonlinear optical properties. In this work, the need to redefine the standard nonlinear figure of merit in terms of nonlinear phase shift and optical transmission for a given propagation distance is argued. According to this new metric, the devices largely outperform all established platforms for optical modules with a linear footprint in the range of 50–500 µm, which is demonstrated to be an outstanding technological gap. For 85 fs pulses, with carrier wavelength at 1480 nm and sub-µW power levels, a spectral broadening exceeding 80% of the initial bandwidth was recorded over a propagation length of just 50 µm. Leveraging on CMOS-compatible processes and well-established materials such as silicon, silica, and indium tin oxide, the devices bring great promise for developing alternative all-optical devices with unparalleled nonlinear performances within the aforementioned range.

1. Introduction

Integrated nonlinear photonics targets the possibility of controlling light with light over very short propagation distances (of the order of the operational wavelength) and with minimal energy expenditure. The basic motivation behind designing all-optical devices lays on the superior bandwidth of optical modules outperforming the fastest electronics by several orders of magnitude. The quest for the "perfect" nonlinear material (a system that can alter its optical properties - i.e. complex index - by a large amount in an ultra-fast fashion and via a minimum amount

of energy) has recently led to the use of transparent conducting oxides (TCOs) within the near-infrared spectral window, where their real refractive index has been reported to be extremely low ($\mathfrak{R}(n)$ < 0.2).[1–3] This condition is associated with a slow light effect leading to giant nonlinearities, which manifest within the ultra-fast optical regime.[4,5] By using near-zero-index (NZI) thin films (thickness < 1 µm) in out-of-plane configurations, ground-breaking nonlinear experiments have been conducted demonstrating record high-frequency conversion in $\chi^{(3)}$ processes,[6–8] large bandwidth shifts of the wavelength carrier of an ultra-fast pulse,[4,9] and unitary change of the refractive index,[10] just to mention a few. However, due to the absorptive nature of nonlinearities in TCOs, propagation distances of several microns are already prohibitive, thus rendering impossible the straightforward design of all-optical on-chip devices. In-plane modulation of optical signals has been achieved via the electric bias of transparent electrodes in silicon waveguides[11–14] while optical control has also been explored theoretically.[15] In addition to this, enhanced supercontinuum generation[16] and four-wave mixing[17] have been demonstrated in guided modes evanescently coupled with single-layer materials such as graphene. However, the graphene-enhanced waveguides reported in this work target length scales on the order of mm and have only been tested in the CW regime. Other waveguide configurations using 2D materials have also shown optical quenching at ultra-low CW powers when pumped externally.[18] However, these devices operate in the visible range and their temporal response has yet to be reported. In the present work, a low-index thin film of indium tin oxide (ITO: $n = 0.97 + 0.63i$) is deposited on top of silicon nanowires immersed in a FOX cladding on top of a silica substrate. These devices are operated at a central wavelength of 1480 nm, which is within our experimental capability, the closest to the ENZ crossover point of our ITO film (See Appendix A, Supporting Information, for dispersion curves and NZI bandwidth, $n < 1$). Nonlinearities are induced on the single propagating mode via evanescent coupling with an upper nonlinear layer of low-index material. In-coupled pulses, with a time duration of 85 fs and power level just below 1 µW, showed nonlinear self-broadening exceeding 80% with respect to the input spectrum after a propagation distance of only 50 µm. Propagating losses can be almost entirely ascribed to the coupling into

W. Jaffray, S. Stengel, M. Ferrera
Institute of Photonics and Quantum Sciences
Heriot-Watt University, SUPA
Edinburgh, Midlothian EH14 4AS, UK
E-mail: m.ferrera@hw.ac.uk

F. Ali, Z. Guo, S. A. Schulz, A. Di Falco
School of Physics and Astronomy
University of St. Andrews
North Haugh, St Andrews, Fife KY16 9SS, UK

The ORCID identification number(s) for the author(s) of this article can be found under https://doi.org/10.1002/adom.202303199

**ADVANCED
SCIENCE NEWS**

www.advancedsciencenews.com

**ADVANCED
OPTICAL
MATERIALS**

www.advopticalmat.de

Table 1. Values of Kerr nonlinearity (n_2) and loss (α) measured at wavelength (λ) are used to generate curves for bulk materials in Figure 1. FoM provides scalar figure of merit for comparison (defined as FoM = n_2/α).

Material	n_2 [cm^{2}W^{-1}]	α [cm^{-1}]	FoM [cm^{3}W^{-1}]	λ [nm]
Si[29]	4.5×10^{-14}	3.2×10^{-8}	1.4×10^{-6}	1500
SiO$_2$[30]	2.7×10^{-15}	4.6×10^{-7}	5.8×10^{-10}	1550
Graphene[22,23]	1.5×10^{-9}	9.5×10^4	1.6×10^{-14}	1550
SiN[27,28]	2.4×10^{-15}	2.43	9.8×10^{-16}	1550
ITO[8]	2.1×10^{-12}	8.3×10^3	2.6×10^{-16}	1310
Au[24–26]	3.1×10^{-12}	6.7×10^5	5×10^{-18}	630

the NZI layer, and they account for ≈0.03 dB μm^{-1} for a core-to-NZI-layer distance of 170 nm (for details on the waveguide design see Experimental Section). Due to the ultra-low power level employed in our tests, we managed to circumvent silicon's nonlinear losses thus allowing for the use of very well-established material platforms. Our study investigates the intrinsic link between a specific device footprint and the most appropriate material for all optical applications. We also demonstrate that by "diluting" the giant nonlinearities of NZI compounds we can fabricate integrated planar devices with hundreds of microns of propagation distances and unparalleled nonlinear performance for optical modules with equivalent device linear footprint. This offers new alternatives for the design of in-plane all-optical NZI tuneable devices and the realization of optical neural networks and ultra-compact computational photonic units.[19,20]

2. Nonlinear Materials Performance

To fully appreciate the reported results, we start by considering a set of underpinning materials in integrated photonics and their fundamental nonlinear figure of merit FoM = n_2/α, where n_2 is the nonlinear Kerr coefficient and α represents the propagation loss coefficient.[21] In **Table 1**, associated results are reported for the following material systems: graphene[22,23] (representative for 2D materials), gold[24,25] (representative for noble metals), ITO[26] (representative for low-index compounds), silicon nitride[27,28] (representative of nonlinear-absorption-free integrated systems), silicon[29] (most established photonic platform), and silica[30] (cornerstone of long-haul optical data transmission). From the reported data it is immediately apparent how this FoM is limiting and at times misleading in describing nonlinear performances.

For instance, the best nonlinear materials according to Table 1 (highest FoM) are silicon followed by silica glass. The reason for this seemingly superior nonlinear performance refers to the fact that when losses are very low, nonlinear effects can be accumulated over enormous distances thus becoming extremely large in magnitude. However, when the target is an integrated nonlinear chip, kilometers of propagation are not affordable and other material systems must be taken into consideration. Additionally, silicon is affected by other detrimental effects such as two-photon absorption that prevent usability if not at ultra-low power levels. Of course, there are technical solutions to circumvent material limitations and enhance local nonlinearities such as the use of micro-cavities.[21,31,32] However, this comes at the price of a largely

reduced operational bandwidth while sitting outside the scope of the present manuscript. To solve the previously mentioned limitations, a more informative and robust figure of merit is needed. This should still take into consideration both losses and nonlinearities but it should also refer to the propagation length associated with the device size. In this regard, we start by considering the infinitesimal nonlinear phase $d\phi$ accumulated over the infinitesimal propagation length dz defined by $d\phi = \gamma' I(z)dz$, where: $\gamma' = 2\pi n_2/\lambda$ can be seen as a nonlinear gamma parameter for bulk propagation, and $I(z) = I_0 e^{-\alpha z}$ is the simplified Beer–Lambert law for linear loss propagation. It is worth noting that if we are considering a propagating mode, the effective nonlinear gamma parameter takes into account modal overlap with the nonlinear region. From here we can evaluate the overall nonlinear phase shift for a given propagation length as follows:

$$\phi(L) = \int_0^L \gamma' I_0 e^{-\alpha z} dz = \frac{2\pi n_2 I_0}{\lambda \alpha}\left(1 - e^{-\alpha L}\right) \quad (1)$$

If we now multiply the percentage of remaining intensity after propagation by the accumulated nonlinear phase, we can derive a more descriptive figure of merit:

$$\text{FoM}'(L) = \frac{2\pi n_2 I_0}{\lambda \alpha}\left(1 - e^{-\alpha L}\right)e^{-\alpha L} \quad (2)$$

Figure 1 shows FoM'(L) for the same set of materials in Table 1 and an internal input peak intensity of $I_0 = 45$ GWcm^{-2} (the one used in our experiment). The colored bands refer to the lengths at which optical transmissions are between 90% and 10% (See "optical characterization" for extra details on nonlinear parameters evaluation). The peak of each FoM' curve corresponds to the device length at which the output signal is 50% of the input (See Appendix B, Supporting Information for further discussion on FoM'.) With regards to the shape of FoM' we can point out that for lower values of L the FoM' is fundamentally driven by the nonlinearity. On the contrary, for higher values of L, the radiation intensity is larger attenuated, and the function becomes loss-driven. Another interesting consideration can be made by looking at the FoM'/FoM ratio, which results in a constant value divided by the system operational wavelength. This accounts for the fact that for a given Kerr coefficient, nonlinear phase shifts are inherently larger at short wavelengths. Finally, it is worth mentioning that the dashed lines in Figure 1 will be handled later in this work and should be ignored for now.

From Figure 1 several interesting considerations can be made. The first and most immediate one is that the picture reflects the typical device length used for a given material. In fact, NZI nonlinearities are best exploited for out-of-plane configurations in thin films with thicknesses below one micron, SiN nonlinear optical devices perform at their best within tens of centimeters of length, and fused silica nonlinear effect are relevant only after several kilometers of propagation (typically considered detrimental for optical communications). In this picture, Graphene is not scalable, and it is represented by one single point for the atomic monolayer. When taking into consideration silicon two-photon absorption by introducing an intensity-dependent α[33] the material appears to be outperformed at any given length by another relevant material in strike contrast with the indication provided by the standard FoM. Finally, arguably the most
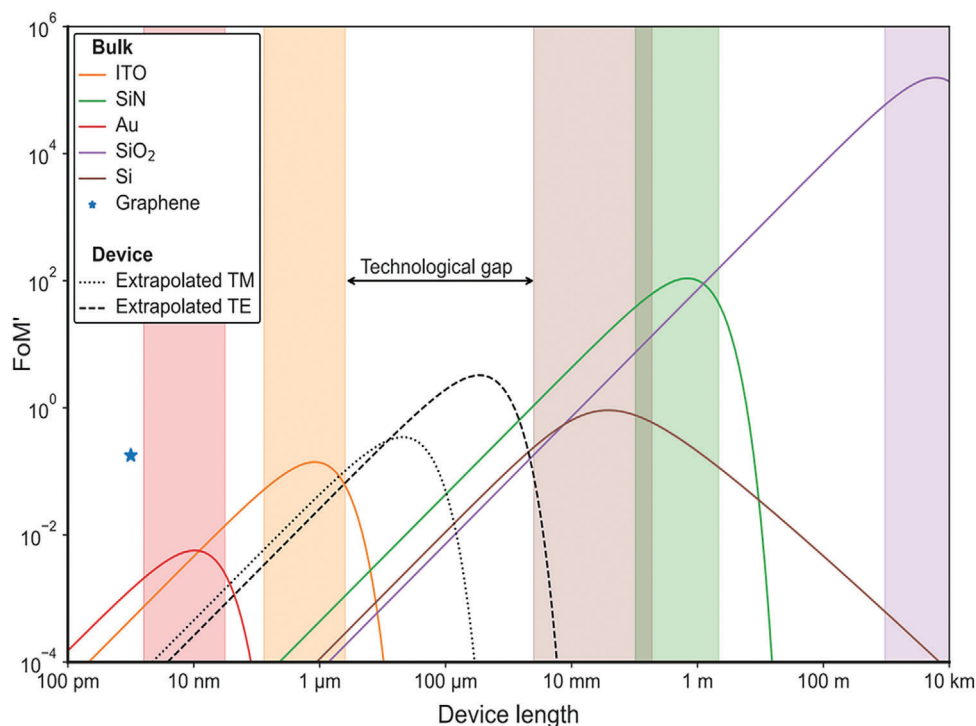
Figure 1. Newly defined nonlinear figure of merit (FoM') for different key materials in integrated photonics as a function of a given propagation distance L. FoM' is defined as the total nonlinear phase shift accumulated by a pulse propagating through a material along a distance L and multiplied by the fraction of remaining light after transmission. Table. 1 provides the reference values used to generate this figure. Solid lines and markers represent the bulk materials: Graphene, silicon (Si), silica (SiO2), gold (Au), silicon nitride (SiN), and indium tin oxide (ITO). Dashed lines represent recovered FoM'(L) for the waveguide geometry experimentally tested for both TM and TE modes. All graphs are produced for a power of 45 GW cm^{-2}, which is the power used inside the NZI waveguides in this experiment. The peak value for all curves corresponds to 50% transmission while colored vertical stripes relates to lengths ranging from 90% to 10% transmission. A direct comparison between the FoM values reported in Table. 1 and the peak values of FoM' in Figure 1 shows the fundamental need to account for optical propagation length to prevent contradictions with common knowledge about optical material properties.
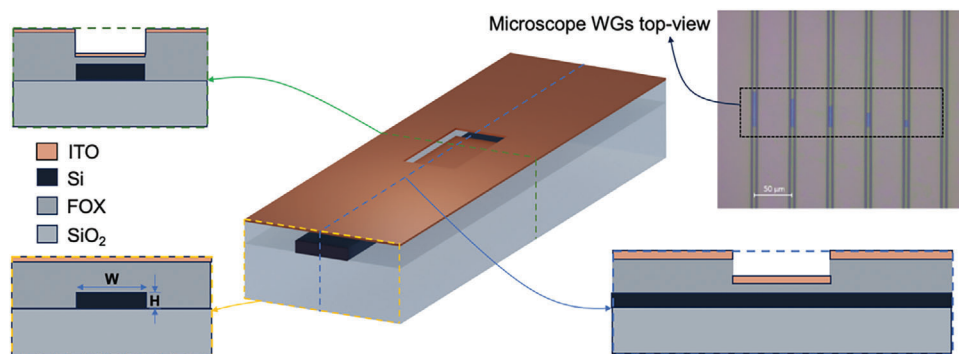
important feature of this plot is that a material gap is immediately apparent for devices in the range 50–500 μm which can be particularly important for any nonlinear integrated module whose functionalities intrinsically require slightly longer propagation length than what is typically targeted in nanophotonics. An example of this might be the emerging use of optical neural networks for which high nonlinearities are required together with a mode mixing region of the order of 100s of μm for telecom wavelength operation.[34] The fundamental question remaining is, how can we fill the previously mentioned technological gap? The following section provides a viable solution to this question.

3. Experimental Section

3.1. Nonlinear Waveguide Design and Fabrication

One of the key goals of the study was to extend the usability of low-index materials over propagation lengths of a few hundred microns. To do so, the proposed strategy was one of "diluting" optical losses by reducing the field coupling into the lossy nonlinear material. However, since this also comes at the cost of reduced nonlinear effects, the effective nonlinear figure of merit of the optical waveguides with lengths of 10–100s microns

will be of fundamental interest. The geometry of the waveguides is reported in **Figure 2**, (not to scale) where a silicon core (W = 3 μm × H = 220 nm cross section) was surrounded by a FOX cladding to create the fundamental guiding line. On top of this structure lies a 50 nm thick layer of low-index ITO while the substrate was silica. All relevant nonlinear effects take place within and along the etched region, here named as "nonlinear trench" for simplicity. The fabrication process of the devices involved the definition of the waveguides using e-beam lithography, followed by spin coating of flowable oxide (HSQ) on the SOI wafer. For all practical purposes, the spacing layer could be assimilated to SiO$_2$. This was followed by e-beam lithography and dry etching to define the nonlinear trenches. The final step was the deposition of the upper (nonlinear) ITO layer by e-beam evaporation. As previously mentioned, ultra-fast optical nonlinearities were activated by the evanescent tail of the propagating mode, which partially coupled into the ITO film. Such coupling could be regulated by varying the size of the silica gap between the waveguide's core and the ITO. To simplify fabrication processes and gain full control over both coupling gap and nonlinear propagation length, etching was performed on the silica cladding before depositing the nonlinear material. Outside the etched region, the ITO film was too far from the core (about 350 nm) to affect mode propagation, as it had been both numerically and experimentally verified.

ADVANCED
SCIENCE NEWS

www.advancedsciencenews.com

ADVANCED
OPTICAL
MATERIALS

www.advopticalmat.de

Figure 2. Nonlinear waveguide layout (not in scale). Device cross sections are shown at both the input region, where ITO is uncoupled to the propagating mode (bottom left), and at the etched area, where nonlinearities are activated (top left). A side view of the waveguide is given on the bottom right which shows the length of the etched region (nonlinear trench). The top right panel provides an optical microscope image of six ITO-coated nonlinear waveguides with various nonlinear trench lengths including a reference waveguide with no trench at all.

Figure 2 also shows a device cross-section before and at the etched region. The top right panel of Figure 2 shows an optical microscope image of six waveguides with nonlinear trenches of varying lengths. The experiments made use of two twin photonic chips with identical layouts, each carrying multiple waveguides with different nonlinear trench lengths, one with the upper ITO layer and one without it. By direct experimental comparison of the two modules, it was ensured that at the operational intensities, silicon's nonlinear absorption was negligible, and spurious silicon nonlinearities were avoided. As the first proof of concept, well-developed material platforms, such as silicon and ITO were chosen. However, it is important to underline that if the above ultra-low power levels are operated to exploit NZI nonlinearities in full, nonlinear absorption-free compounds should be used for the guiding core such as silicon nitride.[21] In addition to this, the low index properties of ITO could also be set almost arbitrarily by either adjusting ITO fabrication parameters[35] or (if an even bigger wavelength shift was required) by using a different TCO.[1,3] Because the optical properties of TCOs could considerably vary with respect to fabrication conditions, for an accurate evaluation of the group velocity dispersion, as well as for the numerical analysis reported in this article, experimentally evaluated dispersion curves for the ITO index were used. The operational wavelength selected for the experiments was at 1480 nm where ITO's real index falls below unity, and the losses remain manageable.

3.2. Experimental Methods

The chip device was tested by using a standard end-fire set-up where light was coupled in and out via two objective lenses. For the nonlinear characterization, a 1 kHz train of 100 fs pulses centered at 800 nm was used to pump an optical parametric amplifier (OPA), generating 85 fs pulses centered at 1480 nm (See **Figure 3** for detailed experimental setup). Input pulses were set to be linearly polarized in either TE or TM polarization via a half wave plate and a polarizer, attenuated, and then focused by a 60 × magnification objective lens onto the facet of the waveguide's core. The output light from the waveguide was collimated via a 40 × magnification objective and then sent to a NIR camera, which was used to optimize coupling and alignment. A flipping mirror, before the NIR camera (not reported in the figure) allowed for "detouring" the beam toward an optical spectrum analyzer for the nonlinear spectral analysis. Additionally, germanium photodiodes were used in conjunction with calibrated beam samplers to monitor beam stability and coupling conditions before and after the waveguides. A tuneable CW laser (not reported in the picture) was used to characterize the waveguide's linear losses as the light was coupled into different waveguides with various nonlinear trench lengths. The waveguides support both fundamental TE and TM modes, with the TM (E field normal to the multilayer interface) being naturally more "interactive" with the nonlinear ITO layer.
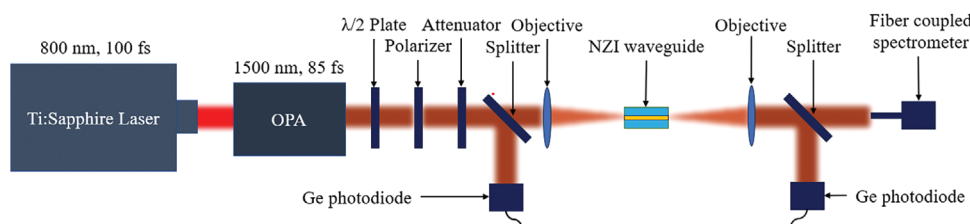
Figure 3. Experimental set-up. Devices were characterized by using a standard end-fire apparatus coupled to a femtosecond laser at the input and NIR cameras and photodiodes at the output. A flipping mirror, before the NIR camera (not reported in the figure) allowed the beam to be detoured towards an optical spectrum analyser for the nonlinear spectral analysis.
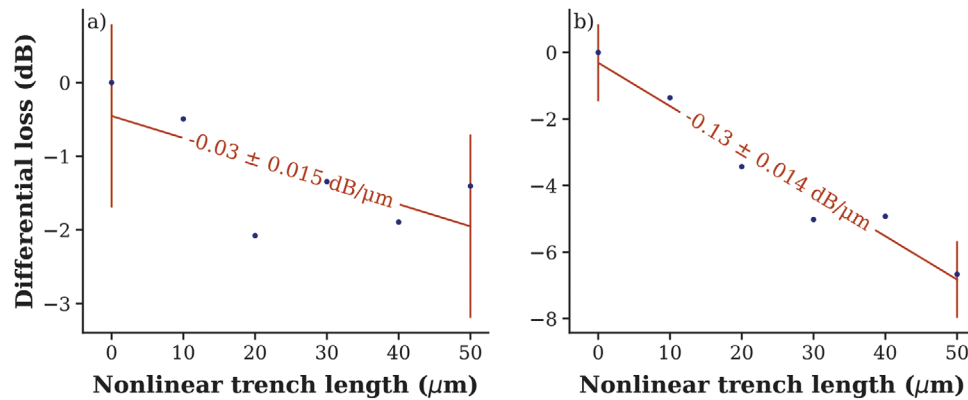
Figure 4. Waveguide propagation losses Vs nonlinear trench length for both a) TE and b) TM modes. The points at channel length equal to zero are evaluated from unetched waveguides and they are taken as a 0 dB loss reference.

4. Results

Propagation losses are experimentally evaluated using the Beer–Lambert law and reported in **Figure 4** for both TE and TM modes. This is done by using input/output power measurements performed on waveguides with different nonlinear trench lengths (3 repetitions of each). With respect to the applicability of the Beer–Lambert law, it is worth mentioning that no real interface is defined by the nonlinear trench and bulk propagation can be considered. The points at length equal to zero are evaluated from unetched waveguides and they are taken as 0 dB loss reference. This allowed for the estimation of the differential loss on multiple nonlinear trenches with different lengths (from 10 to 50 μm with incremental steps of 10 μm - one additional unetched waveguide was also included for calibration purposes) and thus allows for the calculation of propagation losses along the nonlinear region with good accuracy. We should mention that differential loss evaluation does not require pre-knowledge on coupling coefficients

(See Appendix C, Supporting Information for full loss calculations). As expected, losses are considerably higher from the TM configuration and match well with numerical simulations. This will be analyzed in more detail in the "Discussion" session.

Figure 5 provides an overview of the recorded nonlinear spectral broadening for both TE and TM fundamental modes and is instrumental for describing our strategy when evaluating the waveguides effective Kerr index, which is used to plot dashed device curves in Figure 1. For an estimated internal input energy of 45 GWcm^{-2}, both TE and TM input spectra were recorded (blue dots Figure 5). An interpolation curve of these data was then fed into a Generalized Nonlinear Schrodinger Equation (GNLSE) solver to have a numerical evaluation of the output spectra.[36] The numerical model also made use of additional input parameters such as loss, dispersion, mode area, and propagation length, which were attained via Eigenmode simulations of our waveguides (Please see Appendix D, Supporting Information for parameters). The absolute E-fields of the fundamental TE and TM
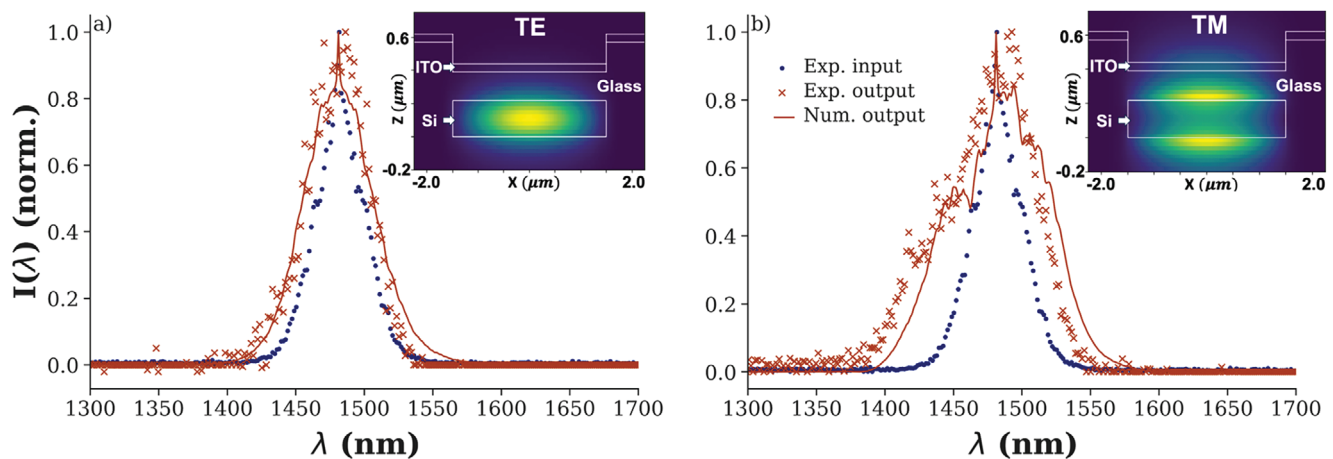

Figure 5. Experimentally recorded spectral broadening after 50 μm of propagation length in our NZI-based waveguide measured for both a) TE and b) TM modes. Blue dots provide the pulse input spectrum as recovered from the OPA prior to waveguide coupling. Red dots refer to the waveguide's experimental output spectra. Several key parameters are set from initial Eigenmode simulations (loss, dispersion, mode area, and propagation length) then effective nonlinearity parameter γ' is estimated by fitting the GNLSE outputs (solid red line) to the experimentally measured output spectra (red crosses). Insets give the absolute electric field for our fundamental TE (panel a) and TM (panel b) modes as recovered by Eigenmode simulations. From these simulations it is evident how the field coupling is considerably higher for the TM mode.

**ADVANCED
SCIENCE NEWS**

www.advancedsciencenews.com

**ADVANCED
OPTICAL
MATERIALS**

www.advopticalmat.de

modes supported by our waveguides are included in the insets of Figure 5. and are also found from Eigenmode simulations (See Appendix E, Supporting Information for full field component breakdown). These simulations were done with Ansys–Lumerical software and used material properties found in the standard literature, except for ITO, which had its permittivity determined via ellipsometry. The geometry consisted of a silicon core (W = 3 μm × H = 220 nm cross section) and a variable thickness cladding of silica with an ITO layer placed on top. Finally, the effective gamma parameter of our system is evaluated from fitting our GNLSE's output (solid red lines Figure 5) to the recorded output spectra (solid red crosses Figure 5). This analysis results in an effective waveguide nonlinearity of $\gamma' = 0.94\times 10^{-11}$ and 1.6×10^{-11} m W^{-1} for the TE and TM modes, respectively. The difference in nonlinearity between these modes can be simply understood by looking into the optical power effectively coupled into the ITO layer for both cases. In this regard, a more detailed analysis is reported in the next paragraph.

5. Discussion

Our experimental analysis is carried out on multiple waveguides with the same spacer thickness of 170 nm (in the following referred as nominal spacer thickness - NST) and different lengths for the nonlinear trench region. This waveguide geometry was chosen via a combination of eigenmode simulations supported by preliminary results on material characterization. By numerical means, we can also confidently extend our analysis to waveguides with different spacer thicknesses. These studies are reported in **Figure 6**, where the top panel (Figure 6a) shows the losses recovered via eigenmode simulations as a function of spacer thickness. Because our simulations do not account for fabrication imperfections, a lower bound attenuation of 0.01 dBμm^{-1} is flatly applied to waveguides for all spacer thickness values. This is necessary to prevent the estimated phase shift from diverging (see the formula for FoM' at Equation 1). The value of 0.01 dB μm^{-1} is not arbitrary, instead it corresponds to the propagation losses experimentally evaluated from testing our 1 cm long waveguides without the upper ITO layer while considering coupling losses from a modal overlap integral analysis. As expected, the TE case has much lower losses than the TM case. This logic follows directly from the middle panel (Figure 6b), where the power coupled into the ITO layer (P$_C$) is plotted Vs the spacer thicknesses. In Figure 6b, as the spacer thickness increases, the modal interaction with the upper ITO layer becomes negligible for both TE and TM, conversely, for very small spacer thicknesses the coupled power becomes similar in magnitude. At NST, the TM mode's power coupling is about twice as strong as the TE mode. The nonlinear analysis for waveguides with different spacer thicknesses is numerically extrapolated from our experimental results for the NST case. In this regard, we decided to follow a simplified approach according to which the power coupled into the ITO layer is considered proportional to the associated nonlinear gamma parameter. This assumption is reasonable as the power coupled into the ITO layer is relatively low, and thus higher-order non-linearities are not activated. It should be noted that a considerable impedance mismatch between our ITO layer and silicon core does not favor coupling into the ITO layer, however, our attained coupling is sufficient to activate nonlinearities. At NST, the ratio
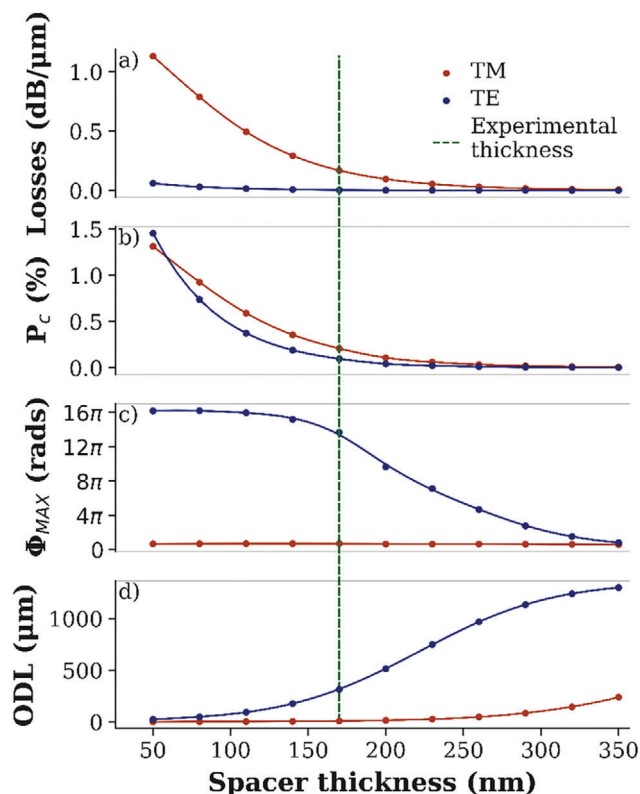
Figure 6. Numerical extrapolation of waveguide properties for different optical coupling with the nonlinear layer. Losses, coupled power (P$_C$ = percentage of total power in the ITO layer), maximal nonlinear phase (ϕ_{max}), and optimal device length (ODL) are plotted as a function of spacer thickness for both TE and TM polarisations in panels (a–d), respectively. The green dashed line highlights the NST points. Plots in panel (a) and (b) are both attained via Eigenmode simulations. The phase shift in panel (c) is found by recording the nonlinear phases evaluated at the maxima of different FOM'(L) curves attained by using Equation (1) for different coupling gaps. Associated gamma parameters for different spacer thicknesses are retrieved by multiplying normalized active power curves by the correspondent TM and TE gamma parameters for the NST case. The normalization over the active power curves is performed over the power values for the NST case. Each point in panel (c) has an associated optimal device length (ODL) which can be attained as guided propagation distance at 3 dB attenuation. ODLs values are reported in panel (d) for completeness. For all curves in Figure 6a trend line is plotted together with numerical points to underline the optical behavior.

of coupled powers of the TE and TM modes (1.83) closely matches the experimentally recovered ratio of TE and TM gamma parameters (1.74) (see green dotted lines in Figure 6). In Figure 6c we plot the nonlinear phase-shift ϕ_{max} evaluated at the maximum of FoM'(L) for different spacer thicknesses for both TE and TM polarisations. The maximum phase shifts are attained via Equation (1) and the correspondent gamma parameters for different spacer thicknesses are retrieved by multiplying normalized active power curves by the correspondent TE and TM gamma parameters for the NST case. The normalization of the active power curves is performed over the power values for the NST case. Each point in Figure 6c is the peak value of a correspondent FoM'(L) curve like those reported in Figure 1, which also corresponds to a specific optimal device length for a given spacer thickness. In

this regard, since the maximum nonlinear phase shift occurs at a transmission of 50%, the optimal device length as a function of spacer thickness can be directly estimated from the loss curves in Figure 6a for a 3 dB attenuation. For the sake of direct quantitative evaluation, we report the plot of optimal device length (ODL) Vs the associated spacer thickness in Figure 6d. It is worth underlying that although the optimal nonlinear propagation length can be set at will by varying the spacer thickness, this would require the fabrication of a new set of devices. However, simply changing the polarization of interest also alters the active power coupled into the nonlinear layer thus changing the FoM'(L) curves whose peak values shift by several tens of microns.

6. Conclusion

Following the general interest in low-index nonlinear technologies and the need for their integration with standard planar photonic modules, we have fabricated and tested a set of nanowires with record high nonlinear figure of merit (here defined as the product of the nonlinear phase shift acquired along a specific propagation length and the fraction of remaining output light). Our devices exploit the evanescent coupling of the propagating field into an upper nonlinear layer of low index ITO to "dilute" optical losses and provide usable nonlinearities over propagation lengths much longer than the penetration depth in bulk TCOs. This allows for direct control over the nonlinear figure of merit by simply changing the coupling gap between the guiding core and the nonlinear layer. Ultra-fast pulse propagation (85 fs) in just 50 µm of our optical interconnects led to a half-π nonlinear phase-shift with a correspondent 80% of spectral broadening. This has been achieved at ultra-low power levels (< 1 µW), thus allowing to circumvent silicon's intrinsic nonlinear absorption. The proposed device configuration enables arbitrarily setting the optimal nonlinear effective length in the range 50 –500 µm, which is proved to be an outstanding technology gap in current integrated photonics. Filling such a gap might be critical for the further development of specific technologies such as integrated optical neural networks for which the degree of integration cannot overcome the requirements for wiring complexity and computational power.

Supporting Information

Supporting Information is available from the Wiley Online Library or from the author.

Conflict of Interest

The authors declare no conflict of interest.

Author Contributions

M.F. and A.D.F. conceived the study and supervised the research activity. W.J. and S.S. performed the numerical study and the nonlinear experiments. F.A. fabricated and characterized the linear properties of the devices and of the deposited materials (with support from Z.H. and S.A.S.). All authors contributed to the preparation of the manuscript.

Data Availability Statement

The data that support the findings of this study are available from the corresponding author upon reasonable request. Plots datapoints are directly accessible at DOI: 10.17861/9d84e279-3661-4722-b29e-ee93e9e846b4

[1] N. Kinsey, C. DeVault, A. Boltasseva, V. M. Shalaev, *Nat. Rev. Mater.* **2019**, *4*, 742.

[2] O. Reshef, I. De Leon, M. Z. Alam, R. W. Boyd, *Nat. Rev. Mater.* **2019**, *4*, 535.

[3] W. Jaffray, S. Saha, V. M. Shalaev, A. Boltasseva, M. Ferrera, *Adv. Opt. Photon.* **2022**, *14*, 148.

[4] E. Lustig, O. Segal, S. Saha, E. Bordo, S. N. Chowdhury, Y. Sharabi, A. Fleischer, A. Boltasseva, O. Cohen, V. M. Shalaev, M. Segev, *Nanophotonics* **2023**, *12*, 2221.

[5] W. Jaffray, F. Belli, E. G. Carnemolla, C. Dobas, M. Mackenzie, J. Travers, A. K. Kar, M. Clerici, C. DeVault, V. M. Shalaev, A. Boltasseva, M. Ferrera, *Nat. Commun.* **2022**, *13*, 3536.

[6] L. Caspani, R. Kaipurath, M. Clerici, M. Ferrera, T. Roger, J. Kim, N. Kinsey, M. Pietrzyk, A. Di Falco, V. Shalaev, A. Boltasseva, D. Faccio, *Phys. Rev. Lett.* **2016**, *116*, 233901.

[7] T. S. Luk, D. de Ceglia, S. Liu, G. A. Keeler, R. P. Prasankumar, M. A. Vincenti, M. Scalora, M. B. Sinclair, S. Campione, *Appl. Phys. Lett.* **2015**, *106*, 151103.

[8] M. Z. Alam, I. De Leon, R. W. Boyd, *Science* **2016**, *352*, 795.

[9] E. G. Carnemolla, W. Jaffray, M. Clerici, L. Caspani, D. Faccio, F. Biancalana, C. Devault, V. M. Shalaev, A. Boltasseva, M. Ferrera, *Opt. Lett.* **2021**, *46*, 5433.

[10] E. Feigenbaum, K. Diest, H. A. Atwater, *Nano Lett.* **2010**, *10*, 2111.

[11] X. Liu, K. Zang, J.-H. Kang, J. Park, J. S. Harris, P. G. Kik, M. L. Brongersma, *ACS Photonics* **2018**, *5*, 4484.

[12] M. Y. Abdelatty, M. M. Badr, M. A. Swillam, *J. Lightwave Technol.* **2018**, *36*, 4198.

[13] J. Baek, J.-B. You, K. Yu, *Opt. Express* **2015**, *23*, 15863.

[14] S. Rajput, V. Kaushik, S. Jain, P. Tiwari, A. K. Srivastava, M. Kumar, *J. Lightwave Technol.* **2020**, *38*, 1365.

[15] J. Gosciniak, Z. Hu, M. Thomaschewski, V. J. Sorger, J. B. Khurgin, *Laser Photonics Rev.* **2023**, *17*, 2200723.

[16] Y. Zhang, J. Wu, Y. Yang, Y. Qu, L. Jia, H. E. Dirani, S. Kerdiles, C. Sciancalepore, P. Demongodin, C. Grillet, C. Monat, B. Jia, D. J. Moss, *Adv. Mater. Technol.* **2023**, *8*, 2201796.

[17] Y. Qu, J. Wu, Y. Yang, Y. Zhang, Y. Liang, H. El Dirani, R. Crochemore, P. Demongodin, C. Sciancalepore, C. Grillet, C. Monat, B. Jia, D. J. Moss, *Adv. Opt. Mater.* **2020**, *8*, 2001048.

[18] M. Lee, H. Hong, J. Yu, F. Mujid, A. Ye, C. Liang, J. Park, *Science* **2023**, *381*, 648.

[19] E. Khoram, A. Chen, D. Liu, L. Ying, Q. Wang, M. Yuan, Z. Yu, *Photon. Res.* **2019**, *7*, 823.

[20] M. Miscuglio, A. Mehrabian, Z. Hu, S. I. Azzam, J. George, A. V. Kildishev, M. Pelton, V. J. Sorger, *Opt. Mater. Express* **2018**, *8*, 3851.

[21] D. J. Moss, R. Morandotti, A. L. Gaeta, M. Lipson, *Nat. Photonics* **2013**, *7*, 597.

[22] E. Hendry, P. J. Hale, J. Moger, A. K. Savchenko, S. A. Mikhailov, *Phys. Rev. Lett.* **2010**, *105*, 097401.

[23] B. Song, H. Gu, S. Zhu, H. Jiang, X. Chen, C. Zhang, S. Liu, *Appl. Surf. Sci.* **2018**, *439*, 1079.

[24] P. B. Johnson, R. W. Christy, *Phys. Rev. B* **1972**, *6*, 4370.

[25] N. Rotenberg, A. D. Bristow, M. Pfeiffer, M. Betz, H. M. van Driel, *Phys. Rev. B* **2007**, *75*, 155426.

[26] R. Boyd, Z. Shi, I. De Leon, *Opt. Commun.* **2014**, *326*, 74.

[27] J. Kischkat, S. Peters, B. Gruska, M. Semtsiv, M. Chashnikova, M. Klinkmüller, O. Fedosenko, S. Machulik, A. Aleksandrova, G. Monastyrskyi, Y. Flores, W. T. Masselink, *Appl. Opt.* **2012**, *51*, 6789.

[28] K. Ikeda, R. E. Saperstein, N. Alic, Y. Fainman, *Opt. Express* **2008**, *16*, 12987.

[29] M. A. Green, M. J. Keevers, *Prog. Photovolt. Res. Appl.* **1995**, *3*, 189.

[30] G. Agrawal, *Applications of Nonlinear Fiber Optics*, Elsevier Science, **2020**.

[31] M. Ferrera, L. Razzari, D. Duchesne, R. Morandotti, Z. Yang, M. Liscidini, J. Sipe, S. Chu, B. E. Little, D. J. Moss, *Nat. Photonics* **2008**, *2*, 737.

[32] J. S. Levy, M. A. Foster, A. L. Gaeta, M. Lipson, *Opt. Express* **2011**, *19*, 11415.

[33] L. Yin, G. P. Agrawal, *Opt. Lett.* **2007**, *32*, 2031.

[34] Y. Shen, N. C. Harris, S. Skirlo, M. Prabhu, T. Baehr-Jones, M. Hochberg, X. Sun, S. Zhao, H. Larochelle, D. Englund, M. Soljačić, *Nat. Photonics* **2017**, *11*, 441.

[35] G. V. Naik, J. Kim, A. Boltasseva, *Opt. Mater. Express* **2011**, *1*, 1090.

[36] J. M. Dudley, J. R. Taylor, *Supercontinuum Generation in Optical Fibers*, Cambridge University Press, Cambridge, England **2010**.